



Improving the rate capability of high voltage lithium-ion battery cathode material $\text{LiNi}_{0.5}\text{Mn}_{1.5}\text{O}_4$ by ruthenium doping



Nilüfer Kiziltas-Yavuz ^{a,*}, Aiswarya Bhaskar ^a, Ditty Dixon ^a, Murat Yavuz ^{a,b}, Kristian Nikolowski ^{a,c}, Li Lu ^d, Rüdiger-A. Eichel ^{e,f}, Helmut Ehrenberg ^{a,b}

^a Karlsruhe Institute of Technology (KIT), Institute for Applied Materials – Energy Storage Systems (IAM – ESS), Hermann-von-Helmholtz-Platz 1, D-76344 Eggenstein-Leopoldshafen, Germany

^b Helmholtz Institute Ulm (HIU) Electrochemical Energy Storage, P.O. Box 3640, 76021 Karlsruhe, Germany

^c Fraunhofer Institute for Ceramic Technologies and Systems IKTS, Winterbergstrasse 28, 01277 Dresden, Germany

^d National University of Singapore, Dept. of Mechanical Engineering, Singapore 117576, Singapore

^e Forschungszentrum Jülich, Institut für Energie- und Klimateforschung (IEK-9), D-52425 Jülich, Germany

^f RWTH Aachen University, Institut für Physikalische Chemie, D-52056 Aachen, Germany

HIGHLIGHTS

- $\text{Li}_x\text{Ni}_{1-x}\text{O}$ was suppressed by Ru-doping as revealed by the presence of such an impurity phase in $\text{LiNi}_{0.5}\text{Mn}_{1.5}\text{O}_4$.
- $\text{LiNi}_{0.4}\text{Ru}_{0.05}\text{Mn}_{1.5}\text{O}_4$ at 1000 °C exhibits excellent electrochemical performances even at high C-rates.
- The mass loadings of the cathodes significantly affect the delivered capacities especially at high C-rate.

ARTICLE INFO

Article history:

Received 7 March 2014

Received in revised form

4 May 2014

Accepted 20 May 2014

Available online 3 June 2014

Keywords:

Spinel

Ruthenium doping

High-voltage cathode

Rate capability

Lithium-ion batteries

ABSTRACT

The citric acid-assisted sol–gel method was used to produce the high-voltage cathodes $\text{LiNi}_{0.5}\text{Mn}_{1.5}\text{O}_4$ and $\text{LiNi}_{0.4}\text{Ru}_{0.05}\text{Mn}_{1.5}\text{O}_4$ at 800 °C and 1000 °C final calcination temperatures. High resolution powder diffraction using synchrotron radiation, inductively coupled plasma – optical emission spectroscopy and scanning electron microscopy analyses were carried out to characterize the structure, chemical composition and morphology. X-ray absorption spectroscopy studies were conducted to confirm Ru doping inside the spinel as well as to compare the oxidation states of transition metals. The formation of an impurity $\text{Li}_x\text{Ni}_{1-x}\text{O}$ in $\text{LiNi}_{0.5}\text{Mn}_{1.5}\text{O}_4$ powders annealed at high temperatures ($T \geq 800$ °C) can be suppressed by partial substitution of Ni^{2+} by Ru^{4+} ion. The $\text{LiNi}_{0.4}\text{Ru}_{0.05}\text{Mn}_{1.5}\text{O}_4$ powder synthesized at 1000 °C shows the highest performance regarding the rate capability and cycling stability. It has an initial capacity of ~ 139 mAh g⁻¹ and capacity retention of 84% after 300 cycles at C/2 charging–discharging rate between 3.5 and 5.0 V. The achievable discharge capacity at 20 °C for a charging rate of C/2 is ~ 136 mAh g⁻¹ ($\sim 98\%$ of the capacity delivered at C/2). Since the electrode preparation plays a crucial role on parameters like the rate capability, the influence of the mass loading of active materials in the cathode mixture is discussed.

© 2014 Elsevier B.V. All rights reserved.

1. Introduction

Among all the cathode materials, the Mn-based spinel materials are potential candidates for high energy and high power density battery applications due to their high operating voltage [1–3]. Moreover, they exhibit high rate performance as a result of the 3D lithium diffusion path formed by 8a tetrahedral and 16c octahedral sites [2,4].

The Ni-doped Mn spinel with the composition $\text{LiNi}_{0.5}\text{Mn}_{1.5}\text{O}_4$ (LNMO) is a highly promising cathode material which shows an impressive electrochemical performance like large reversible capacity at a high operating voltage around 4.7 V where the reversible $\text{Ni}^{2+} \rightleftharpoons \text{Ni}^{4+} + 2\text{e}^-$ redox reactions take place [5–9]. In the ideal $\text{LiNi}_{0.5}\text{Mn}_{1.5}\text{O}_4$ spinel, the oxidation state of Ni and Mn are +2 and +4, respectively, and no Mn ions exist in the trivalent state, which is well-known as Jahn–Teller ion causing structural instability [5,10–12]. However, usually a small amount of Mn^{3+} remains in the compound as a result of oxygen deficiency after the high temperature synthesis process [13–20]. Additionally the

* Corresponding author. Tel.: +49 721 608 28502; fax: +49 721 608 28521.

E-mail address: nilufer.yavuz@kit.edu (N. Kiziltas-Yavuz).

electrochemical performance especially at high rates still needs to be improved to meet the required power density [21–23].

It has been already reported that cation doping on LNMO spinel enhances the reachable capacity, cycling stability and the cycling performance at high C-rates [13,21,22,24,25]. Furthermore, the doping of spinels by 3d or 4d cations can also improve the electrical conductivity and the structural stability [23,26–28]. In 2010, Le et al. studied the influence of tetravalent cation substitution on LNMO [29]. They synthesized $\text{LiNi}_{0.5}\text{Mn}_{1.5-x}\text{M}_x\text{O}_4$, $\text{M} = \text{Ti}$ ($0 < x < 1.3$) and Ru ($0 < x < 1$) samples with solid-state reactions. They have reported that Ti doping decreases the high-voltage electrochemical activity. In contrast, the capacity was maintained and the kinetics were improved by Ru doping. However, no high-rate investigations are reported in this work. Wang et al. reported that the doping of Ru improves the rate capability and also the high-rate cycling stability of LNMO [22,23]. They have synthesized the $\text{LiNi}_{0.5-2x}\text{Ru}_x\text{Mn}_{1.5}\text{O}_4$ ($x = 0, 0.01, 0.03$, and 0.05) samples with solid-state and polymer-assisted methods. Among all the Ru-doped samples, $\text{LiNi}_{0.4}\text{Ru}_{0.05}\text{Mn}_{1.5}\text{O}_4$ showed superior cycling performance (at 10 C charge–discharge rate) and rate capability between 3.0 and 5.0 V. The substitution of a part of divalent Ni ions with tetravalent Ru ions induced some octahedral vacancies [23]. Since the lithium diffusion occurs between tetrahedral sites via vacant octahedral sites, the additional octahedral vacancies formed enhance the feasibility of this process. They reported that $\text{LiNi}_{0.4}\text{Ru}_{0.05}\text{Mn}_{1.5}\text{O}_4$ shows ~100% discharge capacity of its initial discharge capacity when charged with a rate of 0.2 C and discharged from 0.2 C to 2 C. For the high discharge rate of 10 C, it can still retain 89% of its initial discharge capacity. At the highest rate of 10 C they reported discharge capacities of 117 mAh g^{-1} and 121 mAh g^{-1} for solid-state and polymer-assisted synthesized $\text{LiNi}_{0.4}\text{Ru}_{0.05}\text{Mn}_{1.5}\text{O}_4$, respectively.

In this study, sol–gel synthesized LNMO and $\text{LiNi}_{0.4}\text{Ru}_{0.05}\text{Mn}_{1.5}\text{O}_4$ (LNRMO) cathode materials were investigated. The high rate performance studies were carried out up to a discharge rate of 20 C with constant charge rate of 0.5 C. At 10 C discharge rate, the $\text{LiNi}_{0.4}\text{Ru}_{0.05}\text{Mn}_{1.5}\text{O}_4$ sample synthesized at 1000 °C delivered 139 mAh g^{-1} capacity (~100% of the capacity delivered at C/2). Moreover, at 20 C discharge rate, the material delivered a capacity of 136 mAh g^{-1} (~98% of the capacity delivered at C/2) which indicates an excellent high-rate performance of this material. Further details of the electrochemical performance of the Ru-doped material in comparison with the undoped LNMO material are discussed in this manuscript.

2. Experimental

The $\text{LiNi}_{0.5}\text{Mn}_{1.5}\text{O}_4$ and $\text{LiNi}_{0.4}\text{Ru}_{0.05}\text{Mn}_{1.5}\text{O}_4$ materials were synthesized by citric acid-assisted sol–gel method. $\text{LiCH}_3\text{COO} \cdot 2\text{H}_2\text{O}$, $\text{Mn}(\text{CH}_3\text{COO})_2 \cdot 4\text{H}_2\text{O}$, $\text{Ni}(\text{CH}_3\text{COO})_2 \cdot 4\text{H}_2\text{O}$ and $\text{Ru}(\text{CH}_3\text{COO})_2$ precursors were dissolved in a mixture of citric acid and ethylene glycol (1:4 mol mol⁻¹) by heating at 90 °C. Later the solution was heated up to 180 °C to evaporate the excess ethylene glycol from the mixture and to get a transparent gel. The obtained gel was pre-calcined at 400 °C for 5 h to remove the carbon. When the furnace cooled down to room temperature, the mixture was ground in a mortar and then pre-annealed at 600 °C for 24 h in air with intermittent grinding. Until this step, the heating rate was 300 °C h⁻¹. After this step, the materials were separated into two parts for post annealing. One part of each material composition was annealed at 800 °C and the other part at 1000 °C with a heating rate of 600 °C h⁻¹ and holding time <1 min and cooled down to RT slowly in the furnace to obtain the final products. In the following, the samples annealed at 800 °C and 1000 °C are called LNMO-800 °C, LNMO-1000 °C, LNRMO-800 °C and LNRMO-1000 °C.

Diffraction experiments were performed at the high resolution powder diffraction beamline (P02.1) at PETRA-III, DESY, using synchrotron radiation with an energy of 60 keV ($\lambda = 0.20726 \text{ \AA}$) and an exposure time of 2 min. The materials were filled in Kapton capillaries with a diameter of 1.024 mm and the diffraction patterns were acquired using a 2D flat panel detector (Perkin Elmer amorphous-Silicon detector). The obtained 2D images were integrated to 1D diffraction patterns using the X-ray image processing program Fit2D [30]. The structure refinement was performed with Rietveld method using the Fullprof software package [31]. In order to obtain the bulk oxidation states as well as to understand the local coordination of the doped and undoped system X-ray absorption studies (XAS) were conducted. XAS measurements on Mn and Ni K edges were carried out at XAS beamline, ANKA, Karlsruhe and Ru K edge at BM 23 beamline at the ESRF, Grenoble. XAS spectra on electrodes were recorded in transmission geometry for both Mn and Ni K edges. However, due to the low amount of the Ru in the sample, fluorescence geometry was preferred for the Ru K edge measurements. The spectra were processed using the Demeter software package based on IFEFFIT and FEFF [32]. Extended X-ray absorption fine structure analysis (EXAFS) was done using a structural model for $\text{LiNi}_{0.5}\text{Mn}_{1.5}\text{O}_4$ with $Fd\bar{3}m$ space group. It may be noted that an identical first shell structure model was used for generating theoretical feff path (*ab initio* multiple scattering calculations) with corresponding absorbing atom occupying the origin position. For each edge and for each sample, fitting parameter involved a unique amplitude reduction factor or many-body effects (S_0^2) and overall energy parameter (E_0). Moreover, each shell corresponding to an edge or sample was associated with unique temperature factor or EXAFS Debye–Waller factor (DW) and interatomic distance parameter (r). The elemental analysis of the materials was carried out with Inductively Coupled Plasma-Optical Emission Spectroscopy (ICP-OES). The morphology of the particles was analyzed with a Zeiss Supra 55 SEM (Scanning Electron Microscope) with primary energy of 15 keV and an in-lens detector. Before acquiring SEM images, a layer of 8 nm Au/Pd (Au = 80% and Pd = 20%) was sputtered on the surface of the materials using a DC sputtering device (SCD – 050, Baltec) to reduce charging effects.

The $\text{LiNi}_{0.5}\text{Mn}_{1.5}\text{O}_4$ and $\text{LiNi}_{0.4}\text{Ru}_{0.05}\text{Mn}_{1.5}\text{O}_4$ electrodes were prepared by mixing 80% (w/w) of the active material, 10% (w/w) super C 65 carbon (TIMCAL) and 10% (w/w) polyvinylidenefluoride (Solef PVdF 6020 binder, Solvay), in N-methyl-2-pyrrolidone (NMP, Sigma–Aldrich) to get a slurry. The obtained slurry was coated on aluminium foil with wet thicknesses of 120 μm and 300 μm , pre-dried overnight at 80 °C and punched out with the diameter of 1.2 cm. The electrode disks were further dried at 100 °C under vacuum and finally pressed with 8 tons. The mass loadings and thicknesses of the obtained electrodes are ~2 mg cm^{-2} and 12 μm (for 120 μm wet thickness coating) and ~4.5 mg cm^{-2} and 25 μm (for 300 μm wet thickness coating) without including the thickness of Al foil on which the slurry was coated. Two electrode Swagelok®-type test cells were assembled in an argon-filled glove box with lithium foil (Alfa Aesar) as anode, LP30 (1 M LiPF_6 in ethylene carbonate (EC):dimethylcarbonate (DMC) = 1:1) as electrolyte and glass microfiber filters (Whatmann®-GF/D 70 mm Ø) as separator. All electrodes were electrochemically characterized with a VMP3 multi-channel potentiostat (Bio-Logic, France) at 25 °C in the voltage range of 3.5–5.0 V with galvanostatic cycling and cyclic voltammetry (CV) techniques.

3. Results and discussion

Table 1 displays the Li/transition metals ratios of the compounds as determined by ICP-OES. The observed values for Li are slightly smaller than the theoretical values, indicating a small lithium loss

Table 1

The results of ICP-OES analyses.

Sample	Ratio of Li/ transition metals (expected)	Ratio of Li/ transition metals (observed)	Ratio of transition metals Ni:Mn:Ru (observed)
LNMO-800 °C	0.5	0.4951	0.5025:1.5172
LNMO-1000 °C	0.5	0.4956	0.5004:1.5172
LNRMO-800 °C	0.5128	0.5071	0.4048:1.4853:0.0421
LNRMO-1000 °C	0.5128	0.5082	0.3931:1.4853:0.0439

during high-temperature synthesis. Nevertheless, no significant difference is detectable between the samples synthesized at 800 °C and 1000 °C. Fig. 1a–d shows the diffraction patterns of LNMO and LNRMO powders post-annealed at 800 °C and 1000 °C. All the materials have cubic spinel structure and the patterns are indexed with the $Fd\bar{3}m$ space group. An impurity phase with the rock salt $Li_xNi_{1-x}O$ ($Fm\bar{3}m$) structure is obtained for LNMO-800 °C and LNMO-1000 °C powders with phase fractions of ~1% and ~3%, respectively. The existence of this impurity phase is one of the results of oxygen deficiency in the compound which is related to the

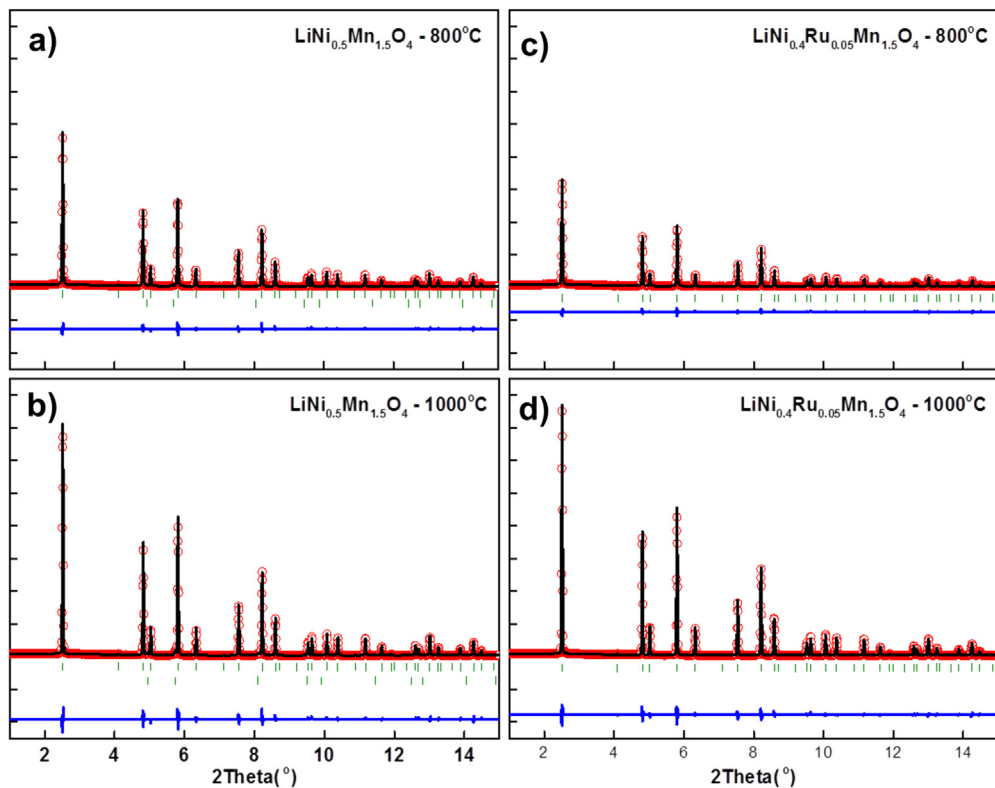


Fig. 1. Synchrotron diffraction patterns of as prepared a) $LiNi_{0.5}Mn_{1.5}O_4$ -800 °C, b) $LiNi_{0.5}Mn_{1.5}O_4$ -1000 °C, c) $LiNi_{0.4}Ru_{0.05}Mn_{1.5}O_4$ -800 °C and d) $LiNi_{0.4}Ru_{0.05}Mn_{1.5}O_4$ -1000 °C samples.

Table 2Rietveld refinement results based on synchrotron diffraction data (space group $Fd\bar{3}m$).

Samples	Atom site	$x = y = z$	a (Å)	Volume (Å 3)	Fraction of impurity phase (%)	Overall temperature factor (B_{ov})	R_{wp} (%)
LNMO-800 °C	[Li] _{8a}	0.125	8.1722(1)	546(1)	1	0.38	6.25
	[Ni] _{16d}	0.500					
	[Mn] _{16d}	0.500					
	[O] _{32e}	0.2630(3)					
LNMO-1000 °C	[Li] _{8a}	0.125	8.1779(1)	547(1)	3	0.39	8.68
	[Ni] _{16d}	0.500					
	[Mn] _{16d}	0.500					
	[O] _{32e}	0.2630(4)					
LNRMO-800 °C	[Li] _{8a}	0.125	8.1830(1)	548(1)	—	0.36	5.12
	[Ni] _{16d}	0.500					
	[Mn] _{16d}	0.500					
	[Ru] _{16d}	0.500					
	[O] _{32e}	0.2631(3)					
LNRMO-1000 °C	[Li] _{8a}	0.125	8.1889(1)	549(1)	—	0.44	6.8
	[Ni] _{16d}	0.500					
	[Mn] _{16d}	0.500					
	[Ru] _{16d}	0.500					
	[O] _{32e}	0.2633(3)					

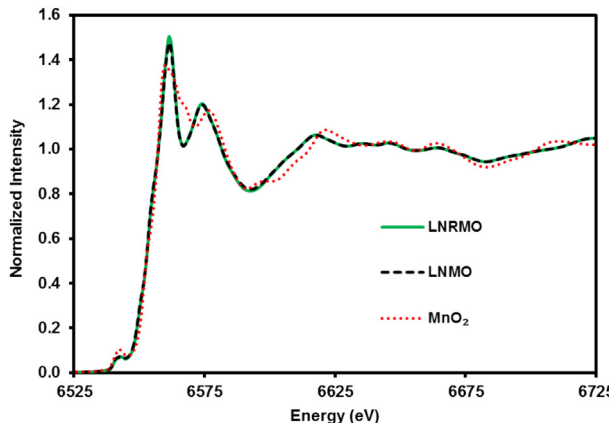


Fig. 2. XANES of the Mn K edge, for $\text{LiNi}_{0.5}\text{Mn}_{1.5}\text{O}_4$ -1000 °C and $\text{LiNi}_{0.4}\text{Ru}_{0.05}\text{Mn}_{1.5}\text{O}_4$ -1000 °C samples, as well as for the reference material MnO_2 .

Table 3
EXAFS fit results obtained for Mn, Ni, and Ru K edges.

	LNMO	LNRMO
rMn–O1 (Å)	1.902(5)	1.903(6)
DW–Mn–O1 (Å ²)	0.0035(6)	0.0032(6)
rMn–Mn (Å)	2.890(5)	2.890(5)
DW–Mn–Mn (Å ²)	0.0036(5)	0.0033(4)
rNi–O (Å)	2.047(4)	2.046(5)
DW–Ni–O (Å ²)	0.0062(5)	0.0056(7)
rNi–Mn (Å)	2.920(3)	2.913(4)
DW–Ni–Mn (Å ²)	0.0053(3)	0.0049(4)
rRu–O (Å)		2.017(9)
DW–Ru–O (Å ²)		0.002(1)
rRu–Mn (Å)		2.940(8)
DW–Ru–Mn (Å ²)		0.0030(9)

high synthesis temperature [14]. Such an impurity phase is not detectable in LNRMO-800 °C and LNRMO-1000 °C samples. This observation implies that Ru doping suppresses the formation of an additional phase. The structural parameters obtained from Rietveld refinement based on the obtained XRD data are listed in Table 2. The lattice parameters increase with increasing synthesis temperature which could be attributed to the oxygen loss from the crystal lattice which in turn increases the Mn³⁺ content in the sample [14]. Moreover, the obtained lattice parameters are larger for the Ru-doped samples than the undoped ones.

To study the influence of Ru doping on the oxidation state of Mn and Ni, X-ray absorption near edge spectra (XANES) region of XAS spectrum were analyzed for LNMO-1000 °C and LNRMO-1000 °C

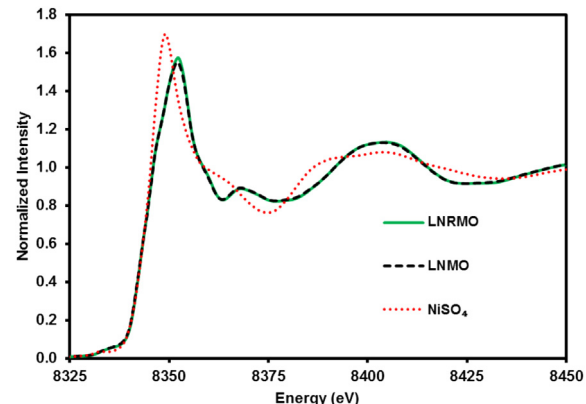


Fig. 4. XANES of the Ni K edge, for $\text{LiNi}_{0.5}\text{Mn}_{1.5}\text{O}_4$ -1000 °C and $\text{LiNi}_{0.4}\text{Ru}_{0.05}\text{Mn}_{1.5}\text{O}_4$ -1000 °C samples, as well as for the reference material NiSO_4 .

samples. The XANES spectra of both doped and undoped samples at Mn and Ni edges were compared with reference materials to obtain the oxidation states of Mn and Ni. Since XANES is a finger print technique, the position of the X-ray absorption edge can be correlated to the oxidation state of the absorbing atom. Therefore, by comparing the XANES region of Mn K edge of both LNMO-1000 °C and LNRMO-1000 °C with the standard MnO_2 , it may be concluded that the Mn in both Ru doped and undoped systems predominantly exist as Mn⁴⁺ (see Fig. 2). It may be stated that, direct evidence of the presence of Mn³⁺ may not be obtained from XANES, as the concentration of Mn³⁺ is too low to be detected. Recently, Rana et al. has correlated the Mn–O bond distance obtained from the extended X-ray absorption fine structure spectra (EXAFS) fitting to the average oxidation state of the Mn [33]. The present EXAFS fitting for both LNMO and LNRMO provided a Mn–O bond distance of 1.90 Å (see Table 3) which may be assigned to an average Mn–O bond lying between Mn^{3.5+}–O and Mn⁴⁺–O. The EXAFS fit for both LNMO and LNRMO at Mn edge is shown in Fig. 3. It should be emphasized that any quantification of Mn³⁺ is limited by the available data range ($\approx 2\Delta k\Delta R/\pi$) where the Δk is the range of Fourier transform and ΔR is the range in R over which the fit is evaluated. By comparing the measured Ni edges with NiSO_4 reference spectra, it can be seen that Ni in both Ru doped and undoped system exist in Ni²⁺ (see Fig. 4). The EXAFS fitting at Ni K edge for both doped and undoped system provided a bond distance of Ni–O, 2.05 Å, which may be assigned to Ni²⁺–O bond distance (see Table 3). The EXAFS fitting for both LNMO and LNRMO spectra at the Ni K edge is shown in Fig. 5. Although an identical structural model was used to fit both Mn and Ni edge a statistically better fit

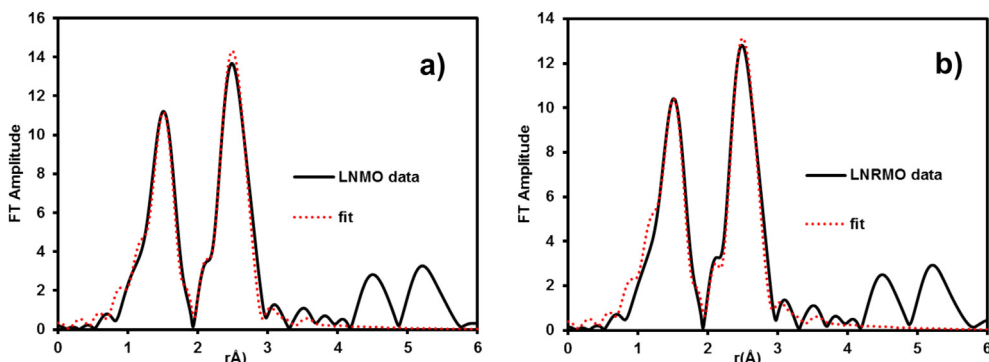


Fig. 3. k^3 weighted EXAFS fitting of the Mn K edge in k range 3–14 Å⁻¹ and r range 1–3 Å a) $\text{LiNi}_{0.5}\text{Mn}_{1.5}\text{O}_4$ -1000 °C, $S_0^2 = 0.57$, $E_0 = -2.4$, reduced $\chi^2 = 232$, b) $\text{LiNi}_{0.4}\text{Ru}_{0.05}\text{Mn}_{1.5}\text{O}_4$ -1000 °C, $S_0^2 = 0.52$, $E_0 = -2.7$, reduced $\chi^2 = 345$.

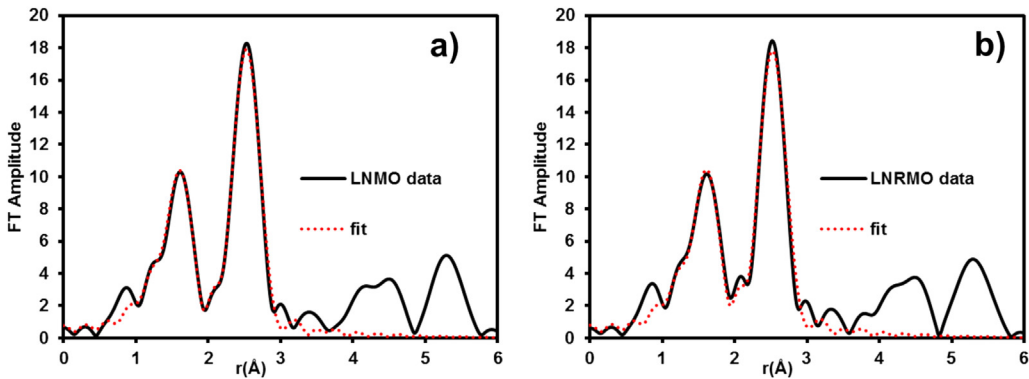


Fig. 5. k^3 weighted EXAFS fitting of the Ni K edge in k range $3\text{--}14\text{ \AA}^{-1}$ and r range $1\text{--}3\text{ \AA}$ a) $\text{LiNi}_{0.5}\text{Mn}_{1.5}\text{O}_4$ -1000 °C, $S_0^2 = 1.0$, $E_0 = -2.92$ reduced $\chi^2 = 39$, b) $\text{LiNi}_{0.4}\text{Ru}_{0.05}\text{Mn}_{1.5}\text{O}_4$ -1000 °C, $S_0^2 = 0.97$, $E_0 = -3.4$, reduced $\chi^2 = 78$.

was observed for the Ni edge. This may be further attributed to the presence of a mixed valance state of Mn which was not taken into account for fitting. To confirm the presence of Ru inside the spinel structure Ru K edge spectra of the Ru doped samples were analyzed. By comparing the Ru K edge XANES spectra of the doped system with the reference spectra of RuO_2 it may be concluded that the Ru inside the doped system exists as Ru^{4+} (see Fig. 6a). Furthermore, to understand the local coordination of the Ru, the EXAFS region of the XAS spectra was analyzed. The Fourier transformation (FT) of the EXAFS spectra to the r space revealed two high amplitude peaks, one at low r value (between 1 and 2 Å) and another at high r value (between 2 and 3 Å) (see Fig. 6b). This is consistent with the FT pattern obtained for Ni as well as Mn edges. Thus, the Ru is expected to be present inside the spinel structure. Finally the EXAFS fitting at the Ru K edge provided a Ru–O bond distance of 2.02 Å and 2.94 Å for Ru–Ni/Mn, respectively, which is the expected for Ru occupying the 16d position in the spinel structure. The larger Ru–Mn/Ni bond distance further explains the larger lattice parameter observed for the LNRMO samples.

SEM images of LNMO-800 °C, LNMO-1000 °C, LNRMO-800 °C and LNRMO-1000 °C are presented in Fig. 7a–d, respectively. The LNMO and LNRMO particles obtained after the annealing at 800 °C lack well defined edges and the particle sizes are in the range of 50–200 nm. In contrast, the particles of the materials synthesized at 1000 °C exhibit pseudo-octahedral shape with smoother surfaces with the size range 1–2 μm and 0.5–1 μm for LNMO-1000 °C and LNRMO-1000 °C, respectively.

Fig. 8 shows the voltage vs. discharge capacity plots of all samples cycled with C/2 charge–discharge rate for the 3rd cycle. The Ru-doped samples exhibit a higher 4 V electrochemical activity than LNMO as revealed from the larger plateau obtained at 3.8–4.4 V voltage range (see inset of Fig. 8). As the 4 V electrochemical activity directly correlates to the amount of Mn^{3+} in the sample, the above observation points out to a higher Mn^{3+} content in LNRMO (0.183 mol) in comparison with LNMO (0.109 mol). This further indicates that the structure can better tolerate the oxygen non-stoichiometry in the presence of Ru, without forming an impurity phase. Moreover, no additional electrochemically active regions are observed which shows that Ru is not participating in the electrochemical reactions.

The CV curves of the 1st and the 10th cycles of LNMO-1000 °C and LNRMO-1000 °C samples are presented in Fig. 9a and b. A reversible electrochemical activity at around 4 V which is attributed to the $\text{Mn}^{3+}/\text{Mn}^{4+}$ redox couple can also be observed here clearly for both materials which is still present after 10 cycles. The two peaks in the region of 4.5–4.9 V during oxidation and reduction processes can be attributed to the $\text{Ni}^{2+} \leftrightarrow \text{Ni}^{3+} \leftrightarrow \text{Ni}^{4+}$ reactions [14–16]. Moreover, the higher 4 V electrochemical activity is clearly visible for the LNRMO-1000 °C sample even after 10 cycles.

The cycling stability results of the first 300 cycles with a C/2 charge–discharge rate in the voltage window 3.5–5.0 V are shown in Fig. 10a. For the materials synthesized at 800 °C, the capacity fading is much higher than the materials synthesized at 1000 °C (see Fig. 10a). The particles of the LNMO-800 °C and

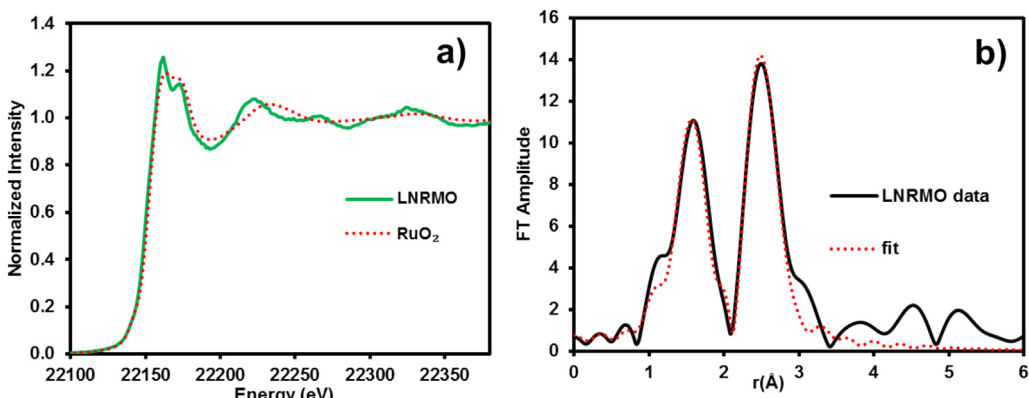


Fig. 6. a) XANES of the Ru K edge for $\text{LiNi}_{0.4}\text{Ru}_{0.05}\text{Mn}_{1.5}\text{O}_4$ -1000 °C, as well as for the reference material RuO_2 k^3 weighted EXAFS fit of the Ru K edge in k range $3\text{--}12\text{ \AA}^{-1}$ and r range $1\text{--}3\text{ \AA}$, $S_0^2 = 0.78$, $E_0 = 3.5$, reduced $\chi^2 = 42$.

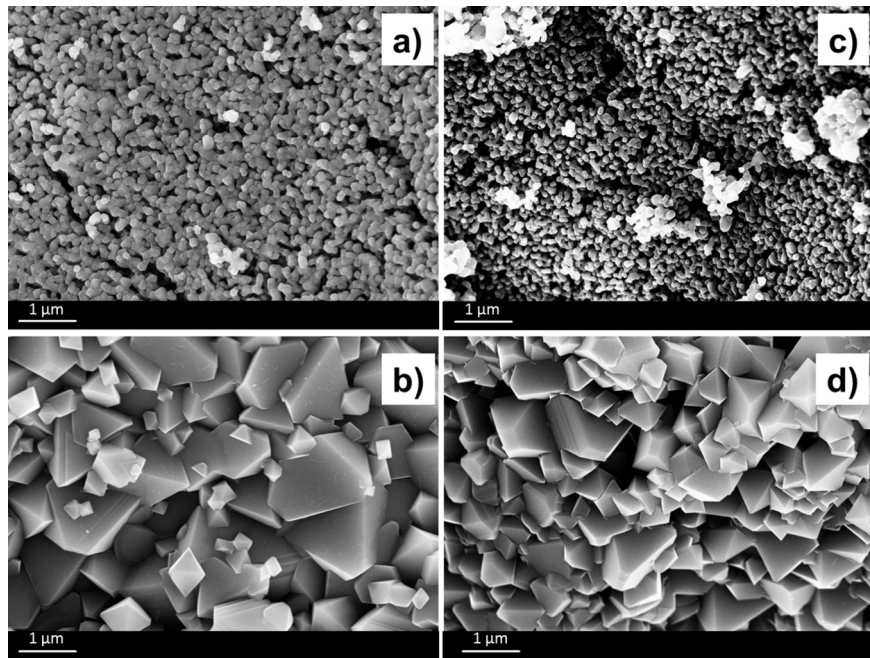


Fig. 7. SEM images of as prepared a) $\text{LiNi}_{0.5}\text{Mn}_{1.5}\text{O}_4$ -800 °C, b) $\text{LiNi}_{0.5}\text{Mn}_{1.5}\text{O}_4$ -1000 °C, c) $\text{LiNi}_{0.4}\text{Ru}_{0.05}\text{Mn}_{1.5}\text{O}_4$ -800 °C and d) $\text{LiNi}_{0.4}\text{Ru}_{0.05}\text{Mn}_{1.5}\text{O}_4$ -1000 °C powders.

LNRMO-800 °C samples are nano-sized and not really well shaped (see Fig. 7a and c). They have a high surface area which in contact with the electrolyte may cause undesirable side reactions and results in poor cycling performance [34]. In contrast, the capacity retention is higher for the materials synthesized at 1000 °C which could be attributed to the bigger particle size with pseudo-octahedral shape, smooth surface and reduced surface area available for parasitic reactions. Fig. 10b shows the 300th discharge curves for all four samples where the high capacity losses of the LNMO-800 °C and LNRMO-800 °C samples are clearly visible, and the 4 V plateau almost vanishes for both samples. In addition, the high-voltage plateaus (~4.7 V) diminish for both samples and are almost absent for LNRMO-800 °C. However, it

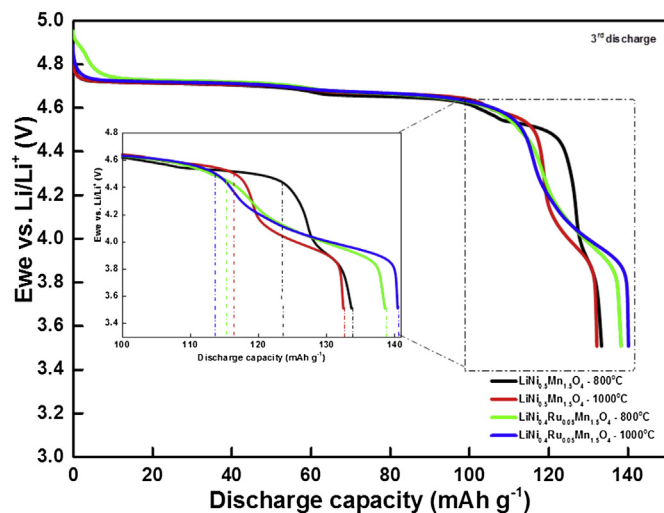


Fig. 8. Voltage vs. 3rd discharge capacity curves of $\text{LiNi}_{0.5}\text{Mn}_{1.5}\text{O}_4$ -800 °C (black), $\text{LiNi}_{0.5}\text{Mn}_{1.5}\text{O}_4$ -1000 °C (red), $\text{LiNi}_{0.4}\text{Ru}_{0.05}\text{Mn}_{1.5}\text{O}_4$ -800 °C (green) and $\text{LiNi}_{0.4}\text{Ru}_{0.05}\text{Mn}_{1.5}\text{O}_4$ -1000 °C (blue) cathodes cycled at a charge discharge rate of C/2 in a voltage range 3.5–5.0 V. (For interpretation of the references to colour in this figure legend, the reader is referred to the web version of this article.)

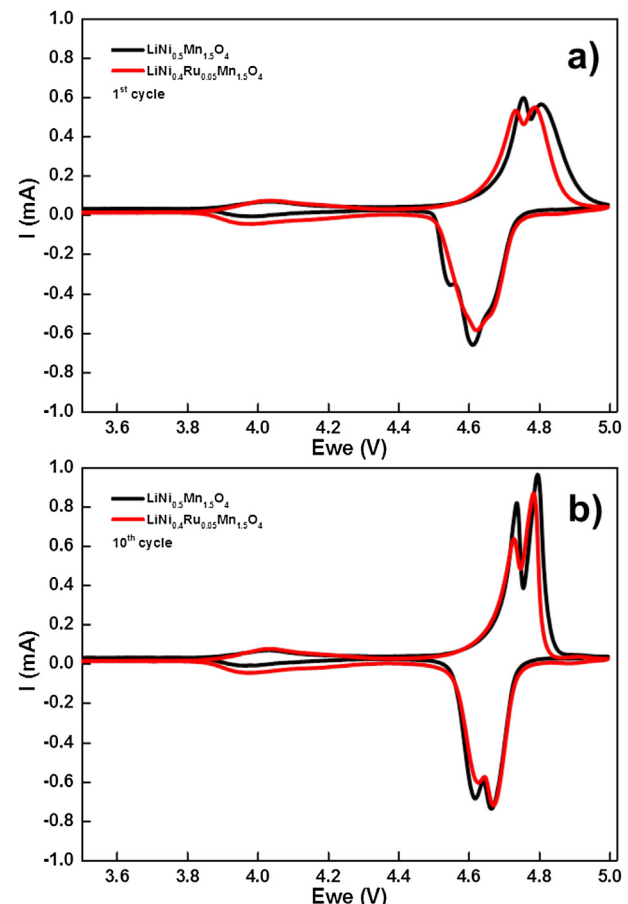


Fig. 9. Cyclic voltammograms of a) 1st cycle and b) 10th cycle of $\text{LiNi}_{0.5}\text{Mn}_{1.5}\text{O}_4$ -1000 °C (black) and $\text{LiNi}_{0.4}\text{Ru}_{0.05}\text{Mn}_{1.5}\text{O}_4$ -1000 °C (red) cathodes with the scan rate of 0.1 mV s^{-1} in a voltage range 3.5–5.0 V. (For interpretation of the references to colour in this figure legend, the reader is referred to the web version of this article.)

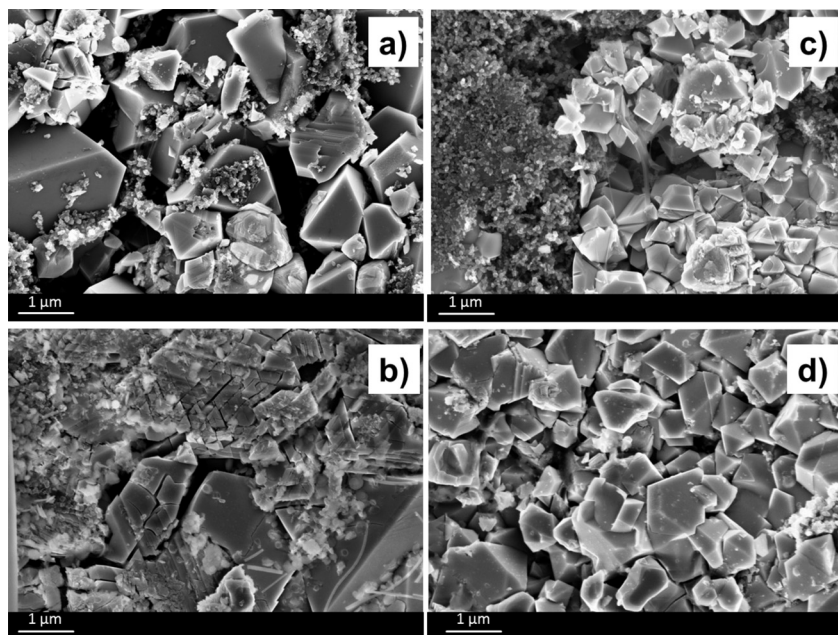
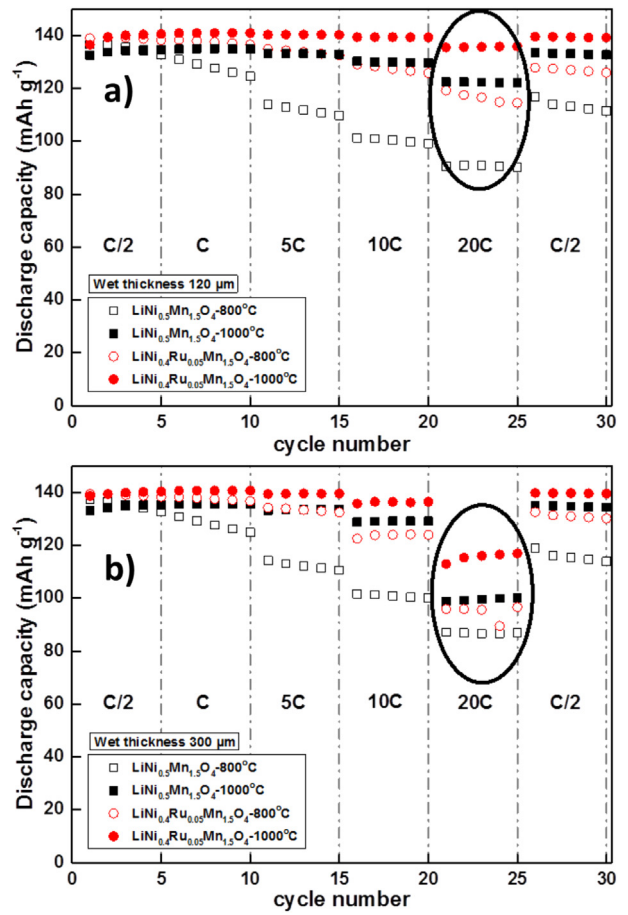
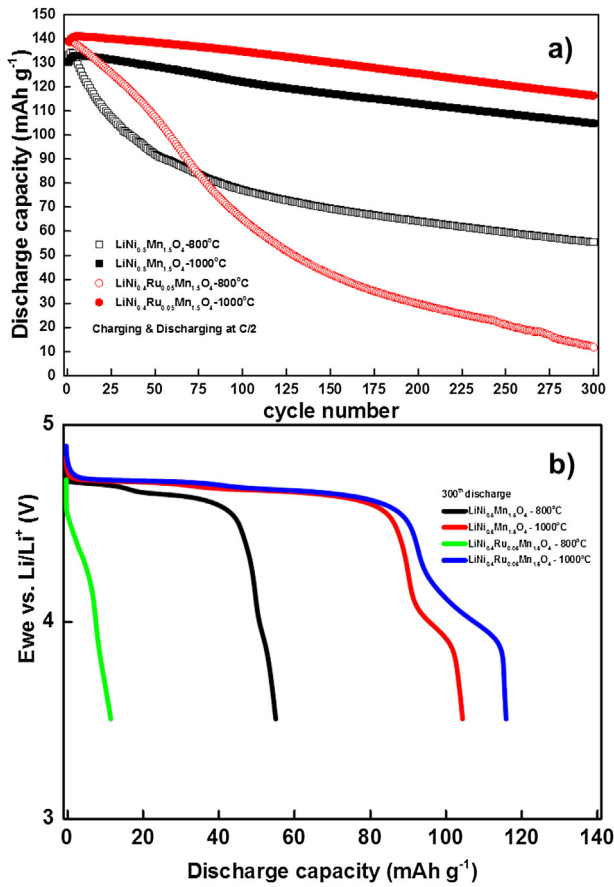


Table 4

The discharge capacities obtained at different C-rates for two different mass loadings.

Sample	Discharge capacity (mAh g ⁻¹) with C/2	The discharge capacities as percentage of the capacity delivered at C/2 for two mass loadings							
		1 C	5 C	10 C	20 C	120 µm	300 µm	120 µm	300 µm
LNMO-800 °C	120 µm	300 µm	120 µm	300 µm	120 µm	300 µm	120 µm	300 µm	120 µm
LNMO-800 °C	136	136	95%	95%	83%	83%	74%	74%	67%
LNMO-1000 °C	134	134	100%	100%	99%	99%	97%	96%	91%
LNRMO-800 °C	139	139	99%	99%	96%	96%	92%	89%	84%
LNRMO-1000 °C	139	139	100%	100%	100%	100%	100%	98%	98%

still exists for the materials synthesized at 1000 °C. Even though LNRMO-1000 °C has a larger 4 V electrochemical activity than LNMO-1000 °C, it has a better cycling stability. The capacity retentions after 300 cycles for LNMO-1000 °C and LNRMO-1000 °C are 79.5% and 84%, respectively.

In order to get a first insight into the ageing mechanism, LNMO-1000 °C and LNRMO-1000 °C have been investigated with SEM before and after 300 cycles (see Fig. 11a–d). The 800 °C synthesized samples were omitted as they exhibit poorer electrochemical performance compared to their high-temperature derivative. Fig. 11a–d show the fresh and the cycled cathodes of LNMO-1000 °C and LNRMO-1000 °C, respectively. It is interesting to note that the LNMO-1000 °C particles undergo severe cracking after cycling. Comparatively much less particle cracks are observed in the case of LNRMO-1000 °C electrodes. One of the reasons of the observed capacity loss in LNMO might be related to this mechanical degradation which increases the total available surface area and in turn results in side reactions such as electrolyte decomposition. Additionally, that can also lead to contact loss which would result in less materials taking part in the electrochemical reaction. This investigation furthermore reveals that ruthenium doping on LNMO also helps to stabilize the structure and morphology to a certain extent.

The high-rate performances of the samples are displayed in Fig. 12a and b. In all cases the charging rate was held constant at C/2 and the discharge rates were varied. Fig. 12a and b present the results of the cathodes prepared with the wet thickness of 120 µm (mass loading is ~2 mg cm⁻² and final electrode thickness is 12 µm without the thickness of Al foil) and with the wet thickness of 300 µm (mass loading is ~4.5 mg cm⁻² and final electrode thickness is 25 µm without the thickness of Al foil), respectively. The discharge capacities as percentages of the capacity delivered at C/2 for the two mass loadings of the four samples are also listed in Table 4. Concerning the materials synthesized at 800 °C, as shown before, the capacity fading of LNRMO-800 °C is much higher compared to LNMO-800 °C (see Fig. 10a) but it delivers higher capacities at high C-rates for both mass loadings. The samples synthesized at 1000 °C have superior high rate-performance compared to the samples synthesized at 800 °C. Among all the materials LNRMO-1000 °C shows the highest absolute capacity even at high C-rates for both mass loadings. This material has the largest unit cell volume (see Table 2) which might support fast diffusion of lithium ions and results in better kinetics of Li insertion/de-insertion to/from the crystal structure. The discharge capacity at 5 C of LNRMO-1000 °C is ~100% of the capacity delivered at C/2. Furthermore, it delivers an absolute capacity of ~139 mAh g⁻¹ for 12 µm thick electrodes and ~136 mAh g⁻¹ for 25 µm thick electrodes at 10 C which are 100% and 98%, respectively, of the capacity delivered at C/2. Hence, up to 10 C, the applied electrode thicknesses and mass loadings do not play a critical role in the capacities delivered. However, at 20 C, the capacities delivered are much more dependent on the mass loadings. At 20 C an absolute capacity of ~136 mAh g⁻¹ (98%) is obtained for 12 µm thick electrodes and ~115 mAh g⁻¹ (83%) for 25 µm thick electrodes.

4. Conclusions

LiNi_{0.5}Mn_{1.5}O₄ and LiNi_{0.4}Ru_{0.05}Mn_{1.5}O₄ materials were successively synthesized with citric acid-assisted sol–gel method and calcination at 800 °C and 1000 °C. The Ru doping in spinel material was confirmed by Ru K edge XAS studies and is expected to be present in 16d sites in the spinel structure. Synchrotron diffraction analyses show that all LNMO powders crystallize in the cubic spinel structure with the $Fd\bar{3}m$ space group but contain small amounts of $Li_xNi_{1-x}O$ impurity at both temperatures. This was suppressed by Ru-doping as revealed by the absence of such an impurity phase in LNRMO which further indicates the increased tolerance of the structure towards an oxygen loss. The amount of Mn³⁺ ions increases with Ru-doping as well as with higher annealing temperatures because of oxygen loss from the crystal lattice. The samples synthesized at 1000 °C have better capacity retentions after 300 cycles at C/2 (79.5% and 84% for LNMO-1000 °C and LNRMO-1000 °C, respectively) than the ones synthesized at 800 °C at the same rate (42% and 8.6% for LNMO-800 °C and LNRMO-800 °C, respectively), which is related to a better crystallinity, superior particle morphology and lower surface area available for parasitic reactions. LNRMO-1000 °C exhibits excellent electrochemical performances even at high C-rates which could be attributed to high unit cell volume and additional octahedral vacancies. It shows the highest discharge capacity (136 mAh g⁻¹ at 20 C) of all samples even though a large 4 V electrochemical activity is observed, which corresponds to the electrochemical activity of Mn³⁺. Additionally the mass loadings of the cathodes significantly affect the delivered capacities especially at high C-rate. To fully understand the structural evolution, *in situ* diffraction experiments during electrochemical cycling and electron paramagnetic resonance (EPR) spectroscopic characterizations are in progress.

Acknowledgement

The authors thank Andrea Voss for elemental analysis using ICP-OES and Udo Geckle for the SEM experiments. This work has benefitted from beamtime allocation by HASYLAB at PETRA III beamline P02.1 in Hamburg. Kind support of the beamline scientists, Stefan Mangold XAS beamline ANKA Karlsruhe, Gleb Parakhonskiy and Olivier Mathon BM 23 ESRF Grenoble is gratefully acknowledged.

References

- [1] J. Liu, Z. Sun, J. Xie, H. Chen, N. Wu, B. Wu, J. Power Sources 240 (2013) 95.
- [2] X. Zhang, H. Zheng, V. Battaglia, R.L. Axelbaum, J. Power Sources 196 (2011) 3640.
- [3] V. Tarnopolskiy, J. Kalhoff, M. Nádherná, D. Bresser, L. Picard, F. Fabre, M. Rey, S. Passerini, J. Power Sources 236 (2013) 39.
- [4] J.-H. Kim, N.P.W. Pieczonka, Z. Li, Y. Wu, S. Harris, B.R. Powell, Electrochim. Acta 90 (2013) 556.
- [5] Q. Zhong, A. Bonakclarpour, M. Zhang, J.R. Dahn, 144 (1997).
- [6] J.S. Park, K.C. Roh, J.-W. Lee, K. Song, Y.-I. Kim, Y.-M. Kang, J. Power Sources 230 (2013) 138.
- [7] T. Okumura, M. Shikano, H. Kobayashi, J. Power Sources 244 (2013) 544.

[8] D. Liu, J. Trottier, P. Charest, J. Fréchette, A. Guerfi, A. Mauger, C.M. Julien, K. Zaghib, *J. Power Sources* 204 (2012) 127.

[9] Z. Zhu, H. Yan, D. Zhang, W. Li, Q. Lu, *J. Power Sources* 224 (2013) 13.

[10] X. Gu, X. Li, L. Xu, H. Xu, J. Yang, Y. Qian, *Int. J. Electrochem. Sci.* 7 (2012) 2504.

[11] S. Bin Park, W.S. Eom, W. Il Cho, H. Jang, *J. Power Sources* 159 (2006) 679.

[12] L. Xiong, Y. Xu, T. Tao, J. Song, J.B. Goodenough, *J. Mater. Chem.* 22 (2012) 24563.

[13] P. Wu, X.L. Zeng, C. Zhou, G.F. Gu, D.G. Tong, *Mater. Chem. Phys.* 138 (2013) 716.

[14] A. Bhaskar, N.N. Bramnik, A. Senyshyn, H. Fuess, H. Ehrenberg, *J. Electrochem. Soc.* 157 (2010) A689.

[15] T. Yoon, S. Park, J. Mun, J.H. Ryu, W. Choi, Y.-S. Kang, J.-H. Park, S.M. Oh, *J. Power Sources* 215 (2012) 312.

[16] Y. Sun, Y. Yang, H. Zhan, H. Shao, Y. Zhou, *J. Power Sources* 195 (2010) 4322.

[17] M. Jo, Y.-K. Lee, K.M. Kim, J. Cho, *J. Electrochem. Soc.* 157 (2010) A841.

[18] A. Bhaskar, D. Mikhailova, N. Kiziltas-Yavuz, K. Nikolowski, S. Oswald, N.N. Bramnik, H. Ehrenberg, *Prog. Solid State Chem.* (2014), <http://dx.doi.org/10.1016/j.progsolidstchem.2014.04.007>.

[19] X. Ma, B. Kang, G. Ceder, *J. Electrochem. Soc.* 157 (2010) A925.

[20] D. Mikhailova, A. Thomas, S. Oswald, W. Gruner, N.N. Bramnik, A.A. Tsirlin, D.M. Trots, A. Senyshyn, J. Eckert, H. Ehrenberg, *J. Electrochem. Soc.* 160 (2013) A3082.

[21] T.-F. Yi, Y. Xie, M.-F. Ye, L.-J. Jiang, R.-S. Zhu, Y.-R. Zhu, *Ionics* 17 (2011) 383.

[22] H. Wang, H. Xia, M.O. Lai, L. Lu, *Electrochim. Commun.* 11 (2009) 1539.

[23] H. Wang, T.A. Tan, P. Yang, M.O. Lai, L. Lu, *J. Phys. Chem.* 115 (2011) 6102.

[24] S.R. Li, C.H. Chen, J.R. Dahn, *J. Electrochem. Soc.* 160 (2013) A2166.

[25] G.B. Zhong, Y.Y. Wang, X.J. Zhao, Q.S. Wang, Y. Yu, C.H. Chen, *J. Power Sources* 216 (2012) 368.

[26] M.V. Reddy, S.S. Manoharan, J. John, B. Singh, G.V. Subba Rao, B.V.R. Chowdari, *J. Electrochem. Soc.* 156 (2009) A652.

[27] T.-F. Yi, Y. Xie, Y.-R. Zhu, R.-S. Zhu, M.-F. Ye, *J. Power Sources* 211 (2012) 59.

[28] M.-W. Jang, H.-G. Jung, B. Scrosati, Y.-K. Sun, *J. Power Sources* 220 (2012) 354.

[29] M.-L.-P. Le, P. Strobel, F. Alloin, T. Pagnier, *Electrochim. Acta* 56 (2010) 592.

[30] A.P. Hammersley, S.O. Svensson, M. Hanfland, A.N. Fitch, D. Hausermann, *High Pressure Res.* 14 (1996) 235.

[31] J. Rodriguez-Carvajal, *Phys. B* 192 (1993) 55.

[32] B. Ravel, M. Newville, *J. Synchrotron Radiat.* 12 (2005) 537.

[33] J. Rana, S. Glathhaar, H. Gesswein, N. Sharma, J.R. Binder, R. Chernikov, G. Schumacher, J. Banhart, *J. Power Sources* 255 (2014) 439.

[34] G.Q. Liu, L. Wen, Y.M. Liu, *J. Solid State Electrochem.* 14 (2010) 2191.